Cylindrical helical cell metamaterial with large strain zero Poisson's ratio for shape morphing analysis

OPEN ACCESS
IOP Publishing
Smart Materials and Structures
Smart Mater. Struct. **32** (2023) 105039 (18pp)
https://doi.org/10.1088/1361-665X/acf96c

Cylindrical helical cell metamaterial with large strain zero Poisson's ratio for shape morphing analysis

Qing Qin* and **Iman Dayyani**

Centre for Aeronautics, School of Aerospace, Transport and Manufacturing, Cranfield University, Bedford MK43 0AL, United Kingdom

E-mail: Q.Qin@cranfield.ac.uk

Received 9 May 2023, revised 7 August 2023
Accepted for publication 13 September 2023
Published 22 September 2023

Abstract

In this paper, a novel cylindrical metamaterial with helical cell exhibiting zero Poisson's ratio (ZPR) in two different directions is introduced. Detailed Computer-aided design modelling of a curved optimised spring element is demonstrated for numerical and experimental analysis. High fidelity finite element models are developed to assess the homogenisation study of Poisson's ratios, normalised Young's modulus and torsion behaviour, demonstrating the curvature effect and independency of mechanical behaviour of cylindrical optimised spring element metamaterial from tessellation numbers. Buckling and frequency analysis of the cylindrical metamaterial with spring element are compared with equivalent shell cylinders. Moreover, experimental analysis is performed to validate the large strain ZPR and deformation mechanism demonstrated in numerical simulations. Finally, radical shape morphing analysis under different bending conditions for cylindrical metamaterial with helical cell is investigated, including deformation and actuation energy and compared with positive and negative Poisson's ratio cylinders formed by honeycomb and auxetic cells.

Keywords: cylindrical mechanical metamaterial, large strain zero Poisson's ratio, 3D helical spring, 3D printing, shape morphing

(Some figures may appear in colour only in the online journal)

1. Introduction

Mechanical metamaterials are artificial structures with precise arrangement cell designs that exhibit mechanical properties superior to natural materials [1]. The rapid development of additive manufacturing technologies has enabled the manufacturing of complex structures in microscopic scales, attracting increasing attention such as Poisson's ratio metamaterials. Negative Poisson's ratio (NPR) metamaterial, also known as auxetic metamaterials, is one of the most widely studied mechanical metamaterials. They exhibit exceptional energy absorption and high fracture resistance due to the expansion of periodic cell structures under compression [2–4]. Zero Poisson's Ratio (ZPR) metamaterials have become more popular since they do not exhibit transverse displacements and undesirable double curvatures under in-plane longitudinal loads and out-of-plane bending moments [5]. This can result in outstanding integration characteristics for complex geometries and boundary conditions, such as 2D planar morphing skins [6].

Gaal *et al* [7] proposed a topological 2D model with blocks comprising two parallel rigid bars with smooth surfaces and a soft and compliant membrane or spring connecting rigid bars. The design exhibits a near-ZPR under compression with

* Author to whom any correspondence should be addressed.

a value of -0.003 ± 0.001 in the experiment. Moreover, they reported that the Poisson's ratio achieved in their design did not depend on the mechanical parameters of the material for small strains. Soman *et al* [8] used digital micro-mirror device projection printing (DMD-PP) to create single-layer and double-layer polyethylene glycol scaffolds composed of semi-re-entrant cells with periodical arrangements to neutralise the in-plane Poisson's ratio within a maximum strain of 0.2. Their tensile experiment and simulations showed that Poisson's ratio was independent of scale and strut materials. Yang and Ma [9] presented 2D metamaterial with self-recovering multi-stable features formed by double-U array of parallel fine crack. Their experimental results showed the design exhibited unstable cyclic near zero to ZPR behaviour in one direction under tension up to a strain value of 2.5.

ZPR ratio behaviour in two directions provides more edge deformation control capability. Gong *et al* [10] introduced and analysed a 2D star shape cellular structure that can exhibit ZPR behaviour in two orthogonal directions. Their research reported that mechanical properties such as Poisson's ratio can be homogenised by tuning the aspect ratio of the cell with unchanged tessellation numbers. Moreover, Naghavi Zadeh *et al* [11] demonstrated a 2D cellular mechanical metamaterial skin formed by Fish-Cells exhibiting ZPR behaviour in two orthogonal in-plane directions. However, the elastic tensile strain range was very small and limited by stress concentration at the joints. Thus, a multi-objective genetic algorithm shape optimisation based on 2D Fish-Cell metamaterial was proposed by Jah and Dayyani [12]. In their study, the detailed joint designs were presented and investigated with parametric studies to successfully reduced 70% Poisson's ratio and increased 75% strain range in one direction.

In compare with 2D ZPR skins, very few research on 3D ZPR metamaterials is investigated. Potential applications for cylindrical ZPR metamaterials include morphing submarines with improved fuel efficiency and minimising weight [13], medical stents [14–16] and soft robotics for works in critical narrow spaces. Liu and Zhang [17] designed a 2D structure with isotropic NPR under large tension and compared it with its 3D cylindrical form. Their research indicated the curvature effect for Poisson's ratio changes for 2D planar and 3D cylindrical structures with identical cell geometry and tessellation numbers. However, the Poisson's ratio of cylindrical metamaterial is significantly affected by cell number in circumferential direction [18–20]. Furthermore, Ling *et al* [21] reported Poisson's ratio for cylindrical metamaterial will be closer to the 2D planar metamaterial once the cell number in circumferential direction reaches to 40.

Gao *et al* [22] presented an analytical method to analyse a cylindrical auxetic microstructure formed by a double-V unit cell exhibiting high stiffness, superior impact resistance and NPR. The chiral structure is one of the most popular designs applied in NPR structures. It has a unique rotation mechanism to expand the structure under tension or compression. The cylinder with a chiral structure provides exceptional advantages compared to the hinge mechanism lattice and traditional hexagonal structures, and the in-plane stress and compressive strength are partially decoupled between the cylinder and ligaments during the deformation mechanism [23]. Furthermore, tension-torsion coupling behaviour is the main characteristic in chiral cylindrical metamaterial under axial loading [24]. Furthermore, Ma *et al* [25] manufactured chiral cylinders by nylon and aluminium, respectively, where the torsion mechanism was independent of the construction materials. Their research showed that the deformation mechanism of local torsion of the cell and the tessellation numbers have an important effect on minimising global compression-torsion torsion.

Qin *et al* [26] presented the first systematic mechanism study for cylindrical Fish-cell metamaterials with two unit cell assembly directions exhibiting ZPR behaviour under a small elastic tensile range in the axial direction and limited by stress concentration. Their research showed the curvature effect and tessellation numbers effect on the homogenisation study of mechanical properties such as Poisson's ratio and effective Young's modulus. Moreover, the linear perturbation study including buckling and frequency was considered with curvature and tessellations influence. Liu *et al* [27] presented an AuxHex cylindrical metamaterial with ZPR behaviours constructed by 4D printing using shape memory polymers with temperature shape programming capability. Their experiment under compression at various temperatures showed that the metamaterial could exhibit ZPR with a compression deformation up to strain 0.5.

ZPR metamaterial is ideal for morphing applications as it has monoclastic behaviour under out-of-plane bending. Morphing cylindrical applications have been studied by different researchers. For instance, Landers *et al* [28] presented aerodynamic testing for a hypervelocity projectile deflectable nose with deflection degrees zero to six degrees with 5% to 13% reduction in drag force at Mach 3.0 and 6.0. Most of the literature studies are constrained in their scope to an aerodynamic response with cylindrical morphing actuation angles under 10 degrees [28–30]. However, Chapkin *et al* [30] presented low aspect ratio cylindrical composites capable of large-scale bending for morphing aerospace applications with a maximum actuation bending of 25 degrees. They investigated circumferentially reinforced composites that minimise actuation energy and radial displacements for out-of-plane bending. Later, Chapkin *et al* [31] designed and optimised high-strain cylindrical composite skins formed by mechanical shell spring and wave shell spring for morphing missile fuselages. They experimentally tested reinforced cylindrical skins up to 20 degrees bending, however, the FEA model shows adhesive layer debonding around 15 degrees bending.

The mechanical behaviour of cylindrical ZPR metamaterial with minimised stress concentration under large tensile strain in axial and radius directions is not well studied. In this work, a novel cylindrical metamaterial with ZPR behaviour formed by helical cell in two directions is introduced. The method of generating the complex geometry in Computer-aided design (CAD) is explained in detail. Experimental and numerical analyses are performed to present the large elastic strain ZPR behaviour of homogenised cylindrical tessellations. Linear buckling and vibration behaviours of the cylindrical helical

cell metamaterials are studied and compared with equivalent shells. The morphology and radical shape morphing capability of the cylindrical metamaterial is demonstrated with different bending conditions. Furthermore, bending mechanisms and actuation energy for ZPR cylindrical metamaterial are compared with positive and NPR cylinders.

2. ZPR metamaterial architecture

Authors have recently demonstrated shape optimised large strain helical structure with 32.7% and 39.1% increment on elastic tensile and compressive strain range compared to linear spring with identical mass and number of coils [32]. Figure 1(a) shows a curved helical cell comprised of four helical elements to demonstrate ZPR behaviour. It is formed by two curved helical elements placed horizontally at the top and bottom highlighted with the indigo background of the helical cell, and another two vertical straight helical elements located on the left and right. Different patterns might be considered for the assembly of unit cell ligaments. The assembly method is based on the authors' previous research results to reduce the manufacturing constraints while maintaining better ZPR trends [32, 33].

The curved optimised helical element demonstrated in figure 1(b) is formed by a curved helical structure with curvature angle α in the middle and two connectors at both ends. Dimensions for the curved helical element can be defined by four parameters: length of the curved optimised helix l, length of the connector l_c, bending angle α and circular cross-section diameter t. The detailed parameters for helical structure can be achieved by the multi objective shape optimisation [32]. Authors have demonstrated comprehensively the parametric study of shape optimisation and corresponding effects on elastic strain range, stress and stiffness [32, 33]. The straight helical element is formed by a straight helical structure and straight connectors with dimensions identical with curved helical element. It must be emphasised that the complex curvatures of cylindrical helical cell metamaterial make the CAD modelling very delicate. The curvature of the helical cell is modified with respect to the variable tessellation numbers in the circumferential direction. A straight helical element is created with a 'wrap curve' function applied to bend the spring element to a specified angle in CATIA V5, curved and straight helical elements are combined to comprise a cell with highly accurate model dimensions. Figure 1(d) demonstrates the cylindrical helical cell metamaterial formed by curved helical cells. Tessellation numbers for numerical and experimental models are presented in 'm*n' format, where 'm' stands for the cell numbers in the circumferential direction and 'n' presents cell numbers in the axial direction of the cylinder. For example, figure 1(d) demonstrates cylindrical helical cell metamaterial with tessellation 10*10, i.e. ten cells in the circumferential direction and ten cells in the axial direction. The length and the diameter of the cylinder can be calculated based on tessellation numbers. The radius of the cylinder can be calculated by $R = \frac{l}{2\sin\alpha}$ where $\alpha = \frac{360}{m}$ and the length of the cylinder $L_c = n(l + 2l_c)$.

3. Zero Poisson ratio cylindrical metamaterial, concept validation

Six Poisson's ratios can be considered for cylindrical systems in 3D continuum mechanics known as: $\nu_{Z\theta}$, $\nu_{\theta Z}$; ν_{ZR}, ν_{RZ}; $\nu_{R\theta}$ and $\nu_{\theta R}$. Considering morphing applications with actuation in axial and radial directions of the cylinder, three Poisson's ratios of ν_{ZR}, ν_{RZ} and $\nu_{\theta Z}$ are essential to study from an integration perspective. Poisson's ratios ν_{RZ} and $\nu_{\theta Z}$ were defined and the calculation methods were obtained by Gao *et al* [22]. Similarly, Poisson's ratio ν_{ZR} has an inverse behaviour with ν_{RZ}, where the negative ratio of axial displacement to the radius change of the cylinder, i.e. $\nu_{ZR} = -\frac{\varepsilon_Z}{\varepsilon_R}$ with the actuation in radius direction.

The numerical method is used to analyse the Poisson's ratio and mechanical behaviour of the cylindrical metamaterial. Simulations are investigated by Abaqus V6.18 with Nylon PA2200 material under elastic properties of Poisson's ratio $v = 0.4$, Young's modulus $E = 1130$ MPa, Yield stress $\sigma_y = 14$ MPa and density $\rho = 930$ kg m^{-3}. Moreover, the plasticity of the material can be found in the author's previous research [22]. Boundary conditions for analysing Poisson's ratio ν_{RZ} and $\nu_{\theta Z}$ of cylindrical metamaterial with helical cells are presented in figures 2(a) and (b), where the left ends of the models are constrained with all degrees of freedom. The right end of the model allows moving only along the longitudinal Z-direction of the cylinder with maximum elastic strains of $\varepsilon_Z = 0.386$. Moreover, boundary conditions for analysing Poisson's ratio ν_{ZR} of cylindrical helical cell metamaterial are presented in figure 2(c), where both ends of the models are constrained with all rotations. The model allows moving only along the radius direction (R axis) of the cylinder with maximum elastic strains of $\varepsilon_R = 0.386$. The models simulated large non-linear effects with three-node quadratic beam elements B32 with circular cross-sections. Mesh convergence study is performed with a minimum global mesh size of 0.75 mm to ensure accurate mesh quality. In calculating the ZPR behaviour of numerical models, an arbitrary radius 'OA' at the middle of cylindrical metamaterial is required, as shown in figure 2. Figure 2(b) shows insignificant displacement in radius 'OA', where models are actuated in the radius directions, demonstrating close to zero values of ν_{ZR}. Poisson's ratio $\nu_{\theta Z}$ with torsion behaviour shown in figure 2(b) with the angle of torsion displacement θ can be considered as: $\theta = \cos^{-1}(\frac{R^2 - R'^2 - d^2}{2RR'})$, where $\vec{R}$ and $\vec{R'}$ are position vectors in original and deformed configurations and $\vec{d}$ is the displacement vector as $\vec{d} = \vec{R'} - \vec{R}$ [22]. Moreover, the distance between points BC in figure 2(c) indicates the cylinder axial length change under strain applied on radius direction for Poisson's ratio ν_{ZR}.

3.1. Homogenisation study for Poisson's ratios

The structural behaviour of metamaterials is influenced by the ratio of unit cell size to cylindrical metamaterial dimension, as well as load and boundary conditions effects. Thus, it is

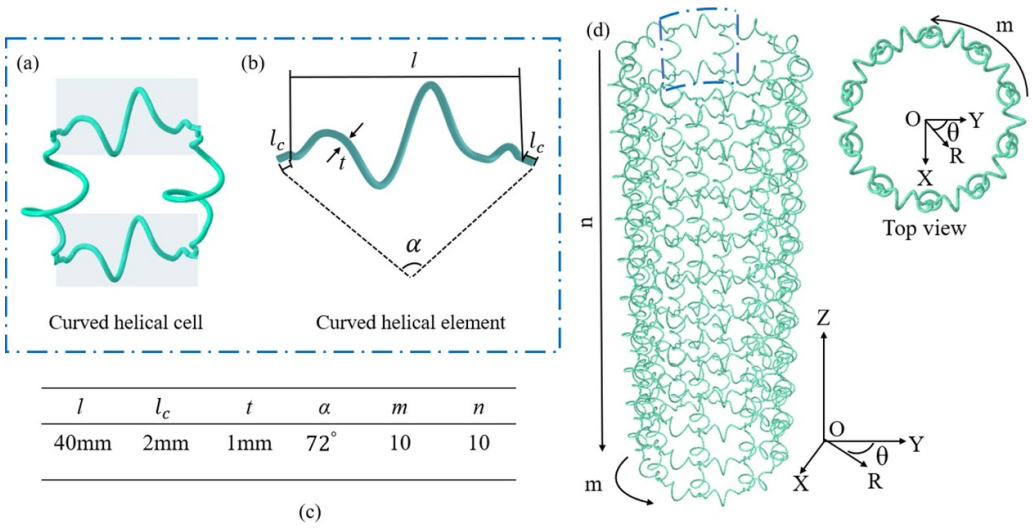

l	l_c	t	α	m	n
40mm	2mm	1mm	72°	10	10

(c)

Figure 1. Dimension of cylindrical helical cell metamaterial, (a) curved helical cell, (b) curved optimised spring element, (c) parameters for curved optimised spring element and cylindrical metamaterial, (d) cylindrical helical cell metamaterial.

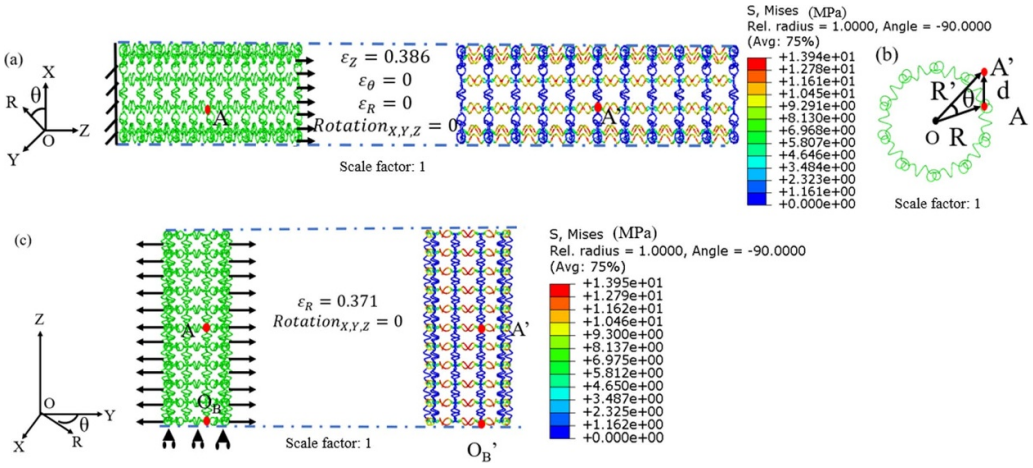

Figure 2. Zero Poisson's ratio simulation of cylindrical metamaterial formed by helical cells, (a) boundary condition for Poisson's ratio ν_{RZ} with metamaterial tessellation number 10^*10. (b) Radial and torsional displacement under boundary condition in (a), (c) boundary condition for Poisson's ratio ν_{ZR} with metamaterial tessellation numbers 10^*10.

essential to perform a homogenisation study with constant size ratios to introduce tessellation numbers demonstrating a behaviour convergence independent from these effects. Different tessellation numbers of 5^*5, 10^*10, 20^*20, 40^*40 and 80^*80 are considered for homogenisation analysis. It should be mentioned that dimensions of unit cells in different tessellation numbers are constant with a cylinder length to diameter ratio greater than three, avoiding short aspect ratio cylinder geometries. Boundary conditions and imposed displacements for Poisson's ratio ν_{RZ} and $\nu_{\theta Z}$ show in figure 3 are identical to what is described in figures 2(a) and (b) with a maximum elastic tensile strain of 0.386. Figure 3 shows extensive strain homogenisation studies of Poisson's ratios ν_{RZ} and ν_{ZR} with different tessellations. Figure 3(a) demonstrates an overall decreasing trend except 5^*5 of positive Poisson's ratio ν_{RZ} by increasing the elastic tensile strain for all tessellation numbers. Tessellation 5^*5 has an increasing trend up to strain 0.2, then decreases until the maximum strain. Moreover, for all tessellations, Poisson's ratio ν_{RZ} is decreasing with tessellation numbers increase. Furthermore, the distance between each line decreases as tessellation numbers increase, illustrating the homogenisation behaviour starts at tessellation numbers 20^*20 with its Poisson's ratio $\nu_{RZ} = 4.3 \times 10^{-2}$ at $\varepsilon = 0.007$ to $\nu_{RZ} = 6.4 \times 10^{-3}$ at $\varepsilon = 0.386$. For instance, Poisson's ratio for tessellation numbers 80^*80 from $\nu_{\theta Z} = 6.9 \times 10^{-3}$ at $\varepsilon = 0.038$ to $\nu_{RZ} = 6.1 \times 10^{-3}$ at $\varepsilon = 0.386$.

Figure 3(b) demonstrates the decreasing trend of the positive Poisson's ratio ν_{ZR} by increasing the elastic strain for all tessellation numbers. Boundary conditions and imposed displacements for Poisson's ratio ν_{ZR} illustrates in table 1 are identical to what is described in figure 2(c) with a maximum elastic tensile strain of 0.371 imposed in the radius direction. Moreover, the stain in cylinder axial directions ε_Z is calculated by the displacement in the Z axis for measuring points A and O_B, i.e $\varepsilon_Z = \frac{\overrightarrow{A'O_B}}{\overrightarrow{AO_B}}$. Homogenisation behaviour

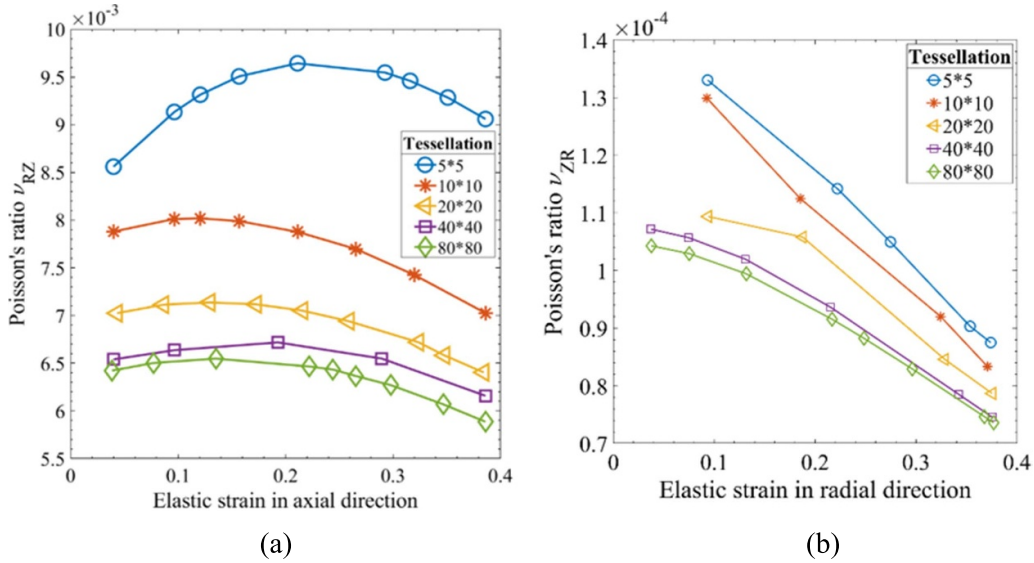

Figure 3. Homogenised trends of Poisson's Ratio with various tessellation numbers for cylindrical zero Poisson's ratio helical cell metamaterials. (a) Poisson's ratio ν_{RZ} at maximum axial tensile strain 0.386, (b) Poisson's ratio ν_{RZ} at maximum radial tensile strain 0.371.

starts at tessellation numbers 20*20 with its Poisson's ratio $\nu_{ZR} = 1.09 \times 10^{-4}$ at $\varepsilon = 0.009$ to $\nu_{RZ} = 7.88 \times 10^{-3}$ at $\varepsilon = 0.371$. It is noticed the Poisson's ratio trend and magnitude between Poisson's ratio ν_{RZ} and ν_{ZR} are very different due to the curvature effect. Poisson's ratio $\nu_{\theta Z}$ in table 3 shows a decreasing convergence trend and homogenised trends with elastic strain increases. For calculation of $\nu_{\theta Z}$, the assumption $\theta = 2\pi$ is made in $\varepsilon_\theta = \frac{u_R}{R} + \frac{1}{R}\frac{\partial u_\theta}{\partial \theta}$ [22]. Moreover, the torsion is caused by the rotational deformation of the joints of the unit cells. The positive Poisson's ratio decreases with tessellation numbers at the same tensile strain and converges at tessellation 20*20 with its Poisson's ratio $\nu_{\theta Z} = 9 \times 10^{-3}$ at $\varepsilon = 0.096$ to $\nu_{\theta Z} = 6.4 \times 10^{-3}$ at $\varepsilon = 0.386$. The change of the Poisson's ratio with tensile strain increases is minimised with tessellation numbers increases. The detailed trend of Poisson's ratio $\nu_{\theta Z}$ is presented in appendix A.

Dissimilar from 3D cylindrical Fish-cell metamaterial [22], cylindrical helical cells metamaterial requires fewer tessellation numbers to reach homogeneity. Although Poisson ratios for cylindrical helical cell metamaterial are larger than cylindrical Fish-cell metamaterial, the elastic strain range for helical cell metamaterial has a more extensive elastic strain range.

3.2. Homogenisation study of normalised Young's modulus

Normalised Young's modulus of cylindrical helical cell metamaterial in the axial direction of the cylinder, i.e. E_{ZZ} can be defined as: $E = \frac{\sigma_Z}{\varepsilon_Z} = \frac{LF_Z}{2\pi Rt\delta_Z}$, where F_Z, δ_Z, L, R and t refer to reaction force, imposed displacement, length and radius of the cylinder as well as elements thickness, respectively. Normalised Young's modulus with respect to the original construction Young's modulus is demonstrated in figure 4 for different tessellations with helical cells. This presents that Young's modulus of the cylindrical metamaterial is dramatically smaller than the original construction material. These very low stiffness and ZPR characteristics can apply to soft robots, medical stents, and morphing wings. The trends of normalised Young's modulus are increasing with elastic tensile strain. This is because the spring stiffness for the coils changes as the diameter of the coils decreases as the tensile strain increases. Moreover, the normalised Young's modulus for all tessellations is very similar. Unlike the homogenisation for Young's modulus of the cylindrical ZPR, Fish-cell metamaterial only homogenised when the tessellation numbers on circumferential direction fixed. The effective Young's modulus for cylindrical ZPR helical cell metamaterial has an identical homogenisation method with 2D Fish-cell metamaterial [11].

4. Buckling analysis

Buckling analysis of cylindrical helical cell metamaterial is advantageous for practical engineering applications of cellular structure with ZPR behaviour. In this section, tessellation numbers effect is considered to study buckling characteristics. Beam elements are used in numerical analysis for the eigenvalue buckling behaviour of metamaterials to minimise the complexity. In these simulations, cell dimensions are fixed while tessellation numbers change, i.e. tessellation numbers are: 5*5, 10*10, 20*20, 40*40 and 80*80. The boundary conditions are fully fixed at one end of the cylinder, the opposite end is coupled with 1 N compression force in the cylinder axial direction. Furthermore, the weight of the metamaterial can be obtained by ABAQUS. Moreover, the buckling behaviour of cylindrical helical cell metamaterial with tessellation 80*80 is compared with an equivalent shell cylinder.

4.1. Buckling modes for cylindrical helical cell metamaterial

Table 2 presents the buckling loads and comprehensive description of mode shapes for various tessellations of the cylindrical metamaterial. The trends of the buckling loads show a non-linear increment as tessellation numbers increase; for

Table 1. Homogenised trend of Poisson's ratio $\nu_{\theta Z}$ with various tessellation numbers for cylindrical zero Poisson's ratio helical cell metamaterial up to maximum elastic tensile strain 0.386.

Tessellation	5*5	10*10	20*20	40*40	80*80
			Poisson's ratio $\nu_{\theta Z}$		
Strain 0.1	5.55×10^{-2}	1.99×10^{-2}	0.90×10^{-2}	0.77×10^{-2}	0.66×10^{-3}
Strain 0.2	2.42×10^{-2}	1.01×10^{-2}	0.76×10^{-2}	0.72×10^{-3}	0.65×10^{-3}
Strain 0.3	1.75×10^{-2}	0.76×10^{-2}	0.71×10^{-2}	0.68×10^{-3}	0.63×10^{-3}
Strain 0.386	1.31×10^{-2}	0.66×10^{-2}	0.65×10^{-2}	0.64×10^{-3}	0.61×10^{-3}

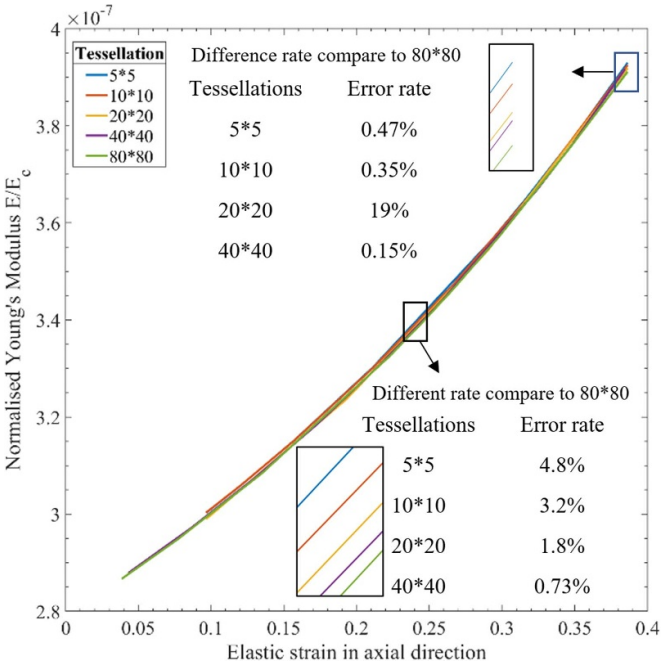

Figure 4. Homogenisation studies of normalised Young's modulus for cylindrical helical cell metamaterial with different tessellation numbers.

example, the buckling load for tessellation 80*80 with a value of 0.55 N is 2.03 times larger than tessellation 5*5 with a value of 0.27 N. This is comparable to the weight ratio of 234.6 for these two tessellation numbers. Thus, the buckling loads are normalised with critical load to the weight of each tessellations model for better understanding. The trend has a dramatic non-linear decreasing behaviour; for instance, tessellation numbers 5*5 with a normalised ratio of 68.878 is 114.6 times larger than 80*80 with the normalised ratio of 0.601. The buckling mode shape for tessellation 5*5 has a bending behaviour for the axis of the cylinder with an undeformed circular cross-section shape at the middle of the cylinder. Similarly, tessellation 10*10 has an undeformed circular cross-section shape at the middle of the cylinder, but its mode shape bends into an 'S' shape. In contrast, other tessellations do not show bending behaviour in the buckling mode shape. The cross-section shapes at the middle of the cylinder for tessellation numbers 20*20 and 40*40 deform into a peanut shape, while tessellation 80*80 has a three-pointed star shape. All tessellations have torsion observed in their mode shapes with values measured at the middle of the cylinder decreasing from 1.11 to 0.02 degrees as tessellation numbers increase. It is noticed the spiral pattern can be observed for tessellation 20*20, 40*40 and 80*80, and the number of the spiral increases with tessellation increases. Thus, from the rotation value measured, the rotation angle decreases with the spiral pattern increases.

Unlike cylindrical Fish-Cell metamaterial, the normalised critical load to the weight of the cylindrical metamaterial with the helical cell is decreased with tessellation numbers increase [22]. The critical buckling load increases with the increase of tessellation number for helical cell metamaterial. However, the decreasing trend for the normalised critical load to the weight indicates the loading capability is not increasing with weight increases. This behaviour is caused by the series connection of the spring that has an inverse relationship with overall stiffness [33]. In other words, the normalised critical load to weight has a convergence behaviour with increasing of tessellation numbers. Furthermore, the cylindrical metamaterial with helical cells experiences larger torsion than with cylindrical Fish-Cell metamaterial. However, the cross-section deformation shapes between these two cylindrical metamaterials are very similar.

The buckling behaviour of a shell cylinder with identical mass is compared with the buckling behaviour of cylindrical metamaterial to discuss the effect of the cell shape on buckling stiffness. The equivalent shell cylinder has identical mass, boundary conditions and dimension but modified 0.1425 mm thickness. The mode shapes of the thin wall shell cylinder are described as axisymmetric folded rings on the cylinder [22] as presented in appendix B. The buckling load for equivalent shell cylinder with value 91.363 N which is 152 times larger than the cylindrical metamaterial.

5. Modal analysis

The fundamental vibration characteristics of this cylindrical metamaterial with regard to its tessellation numbers are discovered by free vibration analysis. Tessellation numbers are identical to those in buckling analysis. Eigenvalue frequency analysis is investigated with a fixed-fixed boundary condition. Ultimately, tessellation 80*80 is compared to an equivalent shell cylinder with identical dimensions and mass but tunned density.

Table 3 demonstrates the first frequencies and mode shapes in the detailed helical cell cylindrical metamaterial description. The trend of the frequencies shows a non-linear decrease with tessellation numbers increases, i.e. the magnitude of the

Table 2. Buckling load and mode shapes for cylindrical helical cell metamaterial.

Tessellation	Critical buckling load (N)	Normalise critical load to weight	Buckling mode shape	Bending of cylinder axis	Cylinder rotation (degree)	Cross section changes at middle
5*5	0.27	68.878	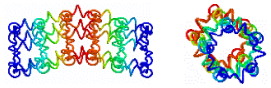	Yes	1.11	No change
10*10	0.38	25.503		Yes	0.51	No change
20*20	0.47	8.076	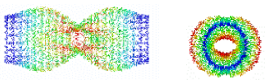	No	0.10	Peanut shape
40*40	0.51	2.217	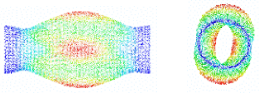	No	0.06	Peanut shape
80*80	0.55	0.601	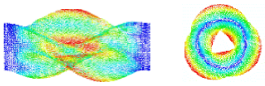	No	0.02	Three-Pointed star

Table 3. The first frequencies and mode shapes for different tessellations of cylindrical metamaterial.

Tessellation	First frequencies (Hz)	First mode shapes	Bending of cylinder axis	Cylinder rotation (degree)	Cross section change
5*5	10.36	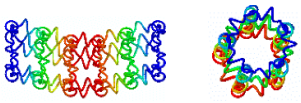	Yes	No	No change
10*10	4.38	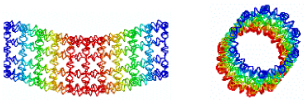	Yes	No	No change
20*20	1.98	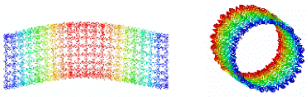	Yes	0.0022	No change
40*40	0.70	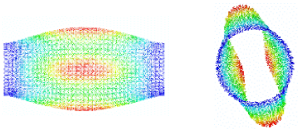	No	0.0014	Peanut shape
80*80	0.28	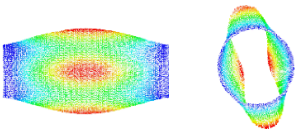	No	0.0005	Peanut shape

frequency for tessellation 5*5 with a value of 10.36 Hz is 37 times larger than tessellation 80*80 with a value of 0.28 Hz. The vibration mode shapes with tessellation 5*5 and 10*10 have a pure bending behaviour for the axis of the cylinder with an undeformed and unrotated circular cross-section shape at the middle of the cylinder. Similarly, tessellation 20*20 shows a bending behaviour for the axis of the cylinder with an unchanged cross-section shape but a tiny rotation 2.2×10^{-3} degrees is detected in the middle of the cylinder. In contrast, tessellations 40*40 and 80*80 do not have to bend mode shapes for the axis of the cylinder at all. The cross-section shapes at the middle of the cylinders for these tessellations are changed to peanut shapes with rotations 1.4×10^{-3} and 5×10^{-4} degrees, respectively.

Table 4 compares the first, third and fifth frequencies and mode shapes between cylindrical metamaterial and equivalent cylindrical shells to evaluate the effect of helical cell architecture on free vibration behaviour. The second and fourth mode shapes and eigenvalues repeat for cylindrical metamaterials and shells. An equivalent shell cylinder for cylindrical metamaterial with tessellations 80*80 is analysed with identical dimensions mass and boundary conditions. However,

Table 4. Comparison of first five frequencies and mode shapes between cylindrical metamaterial with helical cell at tessellation 80*80 and equivalent shell cylinders.

	Tessellation 80*80			Equivalent shell cylinder		
Mode	Frequency (Hz)	Mode shape	Cross section change	Frequency (Hz)	Mode shape	Cross section change
1st &2nd	0.28	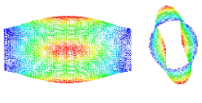		20.43	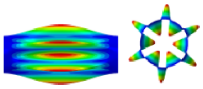	
3rd &4th	0.36	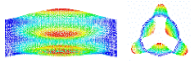		20.64	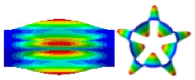	
5th	0.46	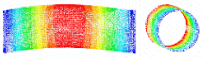		24.17	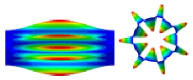	

to maintain the same mass and dimension, only the material density is modified to 132.5 Kg m^{-3}

As shown in table 4, the frequency for cylindrical metamaterial decreases with mode increases, while the frequency increases with mode increases for equivalent shell cylinder. The first and third frequencies of tessellation 80*80 are slightly different from each other, i.e. the ratio of these two frequencies is 1.28. The fifth frequency increases nonlinearly with a value 1.64 times larger than the first frequency. Frequencies of equivalent shell cylinder are approximately 52.5–73.6 times larger than cylindrical metamaterial with a different trend. For example, the first and third frequencies of the equivalent shell are very close to each other with a ratio of 1.01, while the fifth frequency is 1.19 times larger than the first frequency. All mode shapes except the fifth mode shape for cylindrical metamaterial do not show bending. The cross-section at the middle of the cylindrical metamaterial for first and third mode shapes are peanut shape and three-pointed star shape, however, the cross-section shape remains circular. Unlike cylindrical metamaterial, the cross-section shapes of the first, third and fifth modes for equivalent shell cylinders are six, five and seven-pointed star shapes, respectively. Furthermore, the mode shapes for cylindrical metamaterial with helical cell are very similar to cylindrical Fish-cell metamaterial.

6. Experimental analysis

6.1. Manufacturing

The complexity of the curvatures for small scale cylindrical helical cell metamaterial with homogenised tessellations and minimised edge effects challenged the manufacturing. Selective laser sintering (SLS) technology is selected for 3D printing of the cylindrical metamaterial with accomplished fine surface and immensely small tolerance. The 3D printing samples are provided by SDG 3D limited (UK) use Formlabs 3D printer Fuse 1 + 30 W with sintering layer height 110 μms. The main limitation is the minimum thickness of the helical cell with the minimum achievable thickness without a break when moving the model out of the 3D printing machine. Considering all of these limitations including the tensile test area dimensions, a test sample with tessellation 5*5 with an optimised spring element cross-section diameter of 1.8 mm is manufactured as presented in figure 5(a). Moreover, the cross-section between the coil and the connector is slightly smaller than the other parts as illustrated in the orange box in figure 5(b) due to the 3D CATIA design for this very small and complex curvature and the 3D printing tolerance.

6.2. Material characteristics

Material characterisation of PA12 was conducted to validate the numerical models. Thus, five 3D printed dog-bone test specimens with ASTM D638–14 Type 2 standard were tested by tensile experiment to assess the elastic and plastic mechanical properties. The average material properties for PA12 from the tensile test are listed in table 5.

6.3. Tensile structural test

Poisson's ratio and stiffness of the 3D printed model are evaluated by tensile experiment. Grippers at both ends of the cylinder are designed as rigid parts for installing 3D printing model on the tensile machine to imitate the boundary conditions shown in figure 2(a). The test model is installed on a tensile machine as demonstrated in figure 5(b). Digital single lens reflex (DLSR) camera Nikon D7000 is used to capture changes of structure every 30 s to capture the axial displacement and diameter deformation for calculation Poisson's ratio. Moreover, Digital image correlation technique cannot be operated due to the small cross-section thickness of the helical cells and the complex curvature of the model. It is important to place the lens of DLSR camera horizontally to the centre of the model to guarantee that the length and pixels ratio is accurate and consistent. The axial displacement is applied at a 2 mm min^{-1} displacement rate until failure. Poisson's ratio is assessed based on images taken by a DSLR camera, while force–displacement is directly given by tensile machine. The diameter displacement is collected and calculated based on the pixel in the software 'Plot Digitizer', where the ratio between pixel and length is obtained automatically.

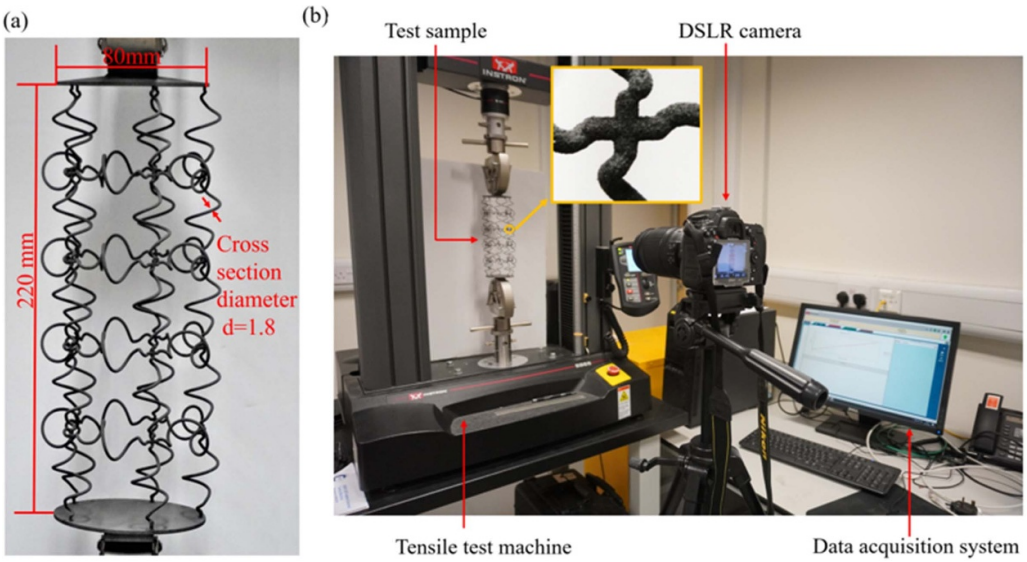

Figure 5. Manufacturing and experimental testing, (a) 3D printing test sample with dimensions highlighted, (b) experimental setup, test machine and data acquisition system.

Table 5. Material elastic properties and plasticity for the 3D printed dog bone samples.

Elastic material property	
Young's modulus E (MPa)	887.675
Poisson's ratio	0.39
Plastic material property	
Strain	Stress (MPa)
0.0216	19.1738
0.0218	19.3048
0.0280	23.7108
0.0357	28.1168
0.0471	32.5229
0.0689	36.9288

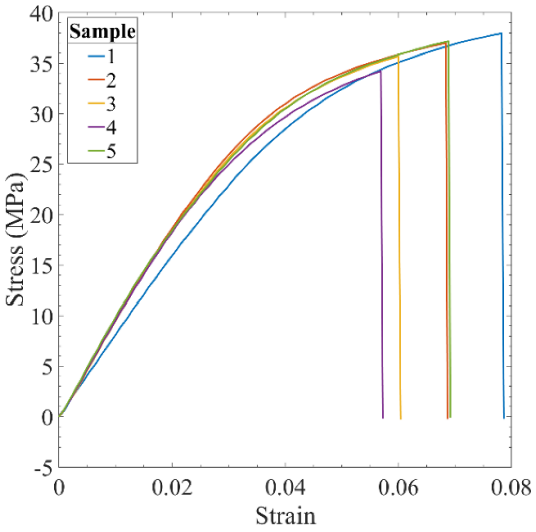

7. Results and discussion

7.1. Poisson's ratio validations

Poisson's ratio validation study between experiment and computational models is presented to demonstrate the reliability of computational models. 3D continuum quadratic solid elements C3D10 with material properties listed in table 5 are used for numerical analysis in ABAQUS. Mesh convergence studies are performed with a global size of 0.5 mm fine mesh is tested and used for discretisation as demonstrated in figure 6(a). Location of measuring points 'A' and 'B' in experimental results are calculated by 'Plot Digitizer' software, which converts the pixel of the experimental images into mathematical coordinates.

Figure 6(b) shows Poisson's ratio as a function of strain for helical cell cylindrical metamaterial. It presents the NPR of helical cell cylindrical metamaterial as increasing steadily as the tensile strain increases and fails at strain 0.92. The numerical and experimental results correlate with Poisson's ratio values. The maximum error between simulations and experiments is approximately 4% at strain 0.846. The major reason for the error in cylindrical metamaterial is measuring method limitation as the deformation of the experiment sample recorded by image processed in 'Plot Digitizer' software. This requires manual selection of the measuring points, with the accuracy of

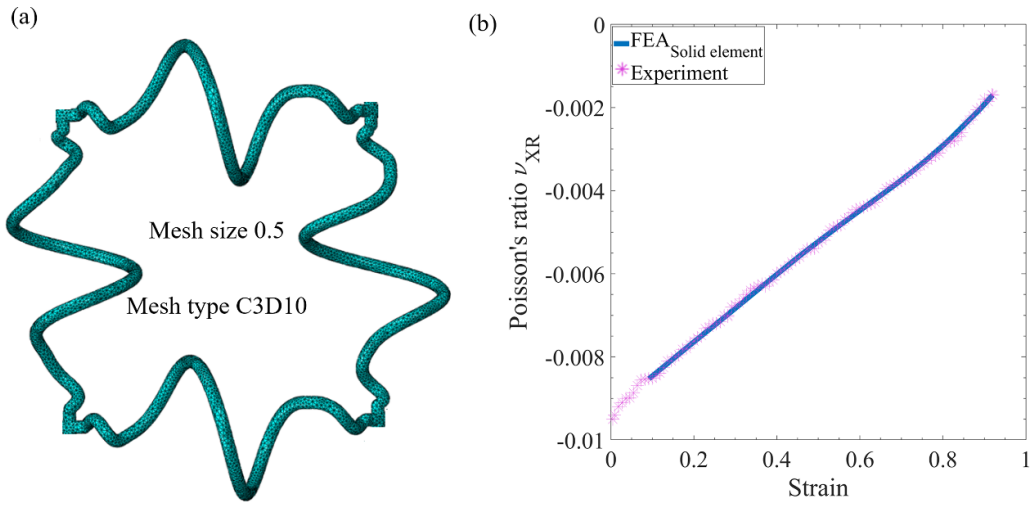

Figure 6. Poisson's ratio as a function of tensile strain, (a) curved helical cell with fine mesh of solid elements, (b) experimental and numerical results of Poisson's ratio VS tensile strain.

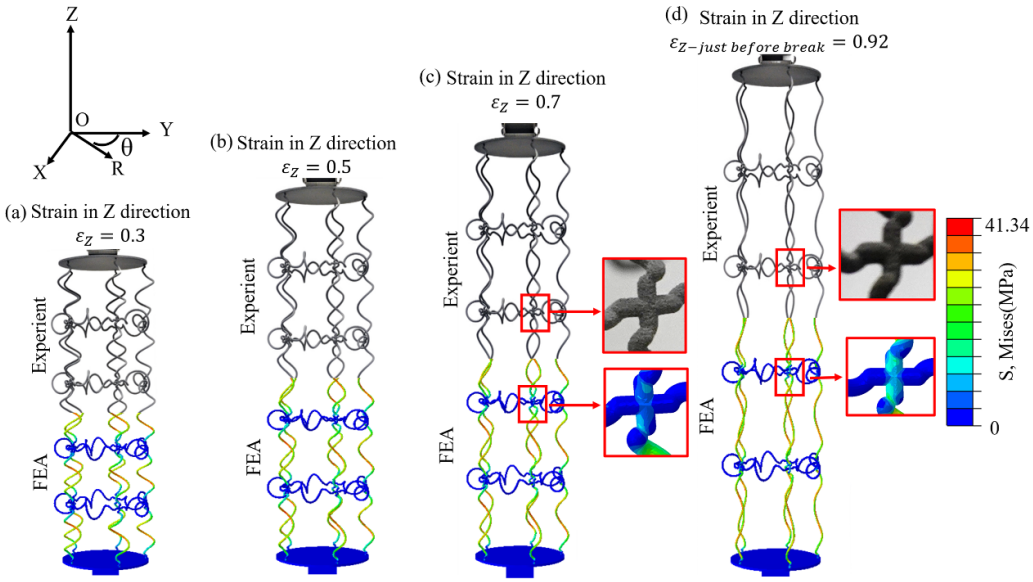

Figure 7. Validation of deformation mechanism in experiment and simulation at the different tensile strain in Z direction, (a) tensile strain 0.3, (b) tensile strain 0.5, (c) tensile strain 0.7, (d) tensile strain 0.92 just before break.

the results depending on the complexity of the geometry and quality of the image.

7.2. Deformation mechanism validation

The deformation mechanism of cylindrical helical cell metamaterial is compared between numerical and experimental models to show the reliability of numerical simulations in a detailed study of the structures. The data for displacement and solid elements discretisation for experimental and numerical models use identical data in section 7.1.

Figure 7 shows similar stress distributions and identical deformation mechanisms in experiment and simulations. The stretch of vertical springs is the typical deformation behaviour for cylindrical helical cell metamaterial in both simulation and experiment. The joints formed by connectors at the ends of coils with a maximum of two degrees anticlockwise rotation observed in figure 7(c) at strain 0.7 are highlighted in red boxes for numerical and experimental models. However, the rotation on the joints is reducing to zero from strain 0.7 to strain 0.92 and detail of the joints for both experiment and numerical is highlighted by boxes in figure 7(d). Moreover, This is because the stretch at the vertical cells distributed the force acting on the joints in different directions up to strain 0.7. However, from strain 0.7 to the failure strain 0.92, the vertical springs had extremely large deformations and tried to deform into a straight line, where the distributed force was aligned in Z direction again. Furthermore, the deformation of horizontal springs is barely seen in the experiment. Only a very tinny displacement can be observed in extracted FEA simulation caused by rotation on the joints. Moreover, figure 7(d) demonstrates similar fracture locations with maximum stress

41.34 MPa at the coils located at the centre of the cylinder and an identical deformation mechanism in the experiment and simulation. Also, the fracture mechanism is constructive material dependent. However, this is beyond the scope of this paper as the attention is on metamaterial architecture.

8. Shape morphing analysis

Cylindrical shape morphing for medical, aerospace and soft robotic applications mainly focuses on bending. It is desired to minimise actuation bending as well as radial deflection and tangential torsion. Shape morphing for positive and NPR cylinders formed by honeycomb and auxetic cells with identical construction material, tessellations, length and diameter are investigated and compared between helical cell cylindrical metamaterial to study the effect of the ZPR features. The detailed dimensions of the auxetic and honeycomb cells are listed in figures 8(c) and (e). This section presents two case studies global bending actuation and theta rotation actuation with boundary conditions in figures 8(a) and 9(a) with tessellation 20*20.

8.1. Global bending actuation

Figure 8 demonstrates the shape morphing under global bending actuation for ZPR, PPR and NPR cylinders. Boundary condition presents in figure 8(a) for global bending actuation with fixed bottom of the cylinder and applying moment at the top of the cylinder along X axis at rotation centre O_c, where the distance between the rotation centre O_c and axis of the cylinder is $R_C = L_c$. Three sets of measuring points place on NPR cylinder with re-entrant cell and ZPR cylindrical helical cell metamaterial at locations $0.25L_c$, $0.5L_c$ and $0.75L_c$to measure the diameter change. However, due to PPR cylinder having more complicated deformation than other cylinders, the measuring points are set at $0.1L_c$, $0.4L_c$, $0.5L_c$, $0.7L_c$, $0.9L_c$. The magnitude of maximum positive and negative strain are present and compared with each other with deformation illustrated.

Figure 8(a) demonstrates the diameter strain as a function of rotation degrees at different measuring point locations for helical cell cylindrical metamaterial with a maximum elastic rotation of 24 degrees. The diameter strain trends increase with the actuation rotation angle increases. The magnitude of the positive diameter strains measure at all locations except $0.25L_c$ are higher than negative diameter strains. Moreover, the magnitude of positive and negative diameter strains at $0.5L_c$ and $0.7L_c$ are almost identical, and the negative diameter strain at $0.25L_c$ is identical to $0.75L_c$. Furthermore, the maximum positive increment on diameter strain is with the value of 0.27 at location $0.25L_c$ and maximum rotation angle 24 degrees, while the largest negative diameter strain at a rotation angle 24 degrees is with value 0.07 at location $0.75L_c$. Figure 8(b) demonstrates the deformation for the global bending actuation of cylindrical metamaterial with helical cells in different views. A bending behaviour without significant diameter change is observed from rotation degrees 0–10 degrees in YZ and XZ planes. However, a significant shrink is observed at a rotation angle of 24 degrees in YZ plane at the middle of the cylinder $0.5L_c$. Additionally, a significant diameter increase is noticed at a rotation angle of 24 degrees in XZ plane in the middle of the cylinder. The cross-section shapes with an actuation rotation angle 24 degrees at all measuring locations are deforming to an oval shape and exaggerated with scale factor three. It is noticed that the maximum and minimum diameter strains are measured along Y and X axis. Moreover, it is noticed for all measuring points besides $0.25L_c$, the maximum diameter strains are measured along Y axis.

Figure 8(c) presents an NPR cylinder with a maximum 13.4 degrees elastic actuation rotation angle, which is 1.7 times smaller than cylindrical metamaterial with helical cells. Similar to cylindrical helical cell metamaterial, the magnitudes for diameter strains are increasing with elastic actuation rotation angle increases. Moreover, for all measuring points except $0.25L_c$, the maximum magnitudes of the diameter strain are positive. The magnitude of the maximum and minimum diameter strain at $0.5L_c$ and $0.75L_c$ are very close, while the diameter strain at $0.25L_c$ are very different. Furthermore, the maximum positive diameter strain is with value of 0.14 at location $0.25L_c$ and rotation angle 13.4 degrees, which is two times larger than cylindrical helical cell metamaterial at the same rotation angle. The maximum negative diameter strain is with a value -0.06 at location $0.5L_c$ and rotation angle 13.4 degrees, which is 1.5 times larger than cylindrical helical cell metamaterial at the same rotation angle. Figure 8(d) demonstrates the deformation for the global bending actuation of the NPR cylinder with re-entrant cell. Bending behaviour with insignificant diameter change is observed from rotation degrees 0–5 degrees in YZ and XZ planes with no significant diameter change. A significant decrease in diameter is observed from the compression tension side at the middle of the cylinder with a rotation angle 13.4 degrees in YZ plane. The cross-section shapes with an actuation rotation angle 13.4 degrees at all measuring locations are deforming to an oval shape and exaggerated with scale factor three. Similar to cylindrical spring cell metamaterial, for all measuring points besides $0.25L_c$, the maximum diameter strains are measured along Y axis and the minimum diameter strains are measured along X axis. Moreover, the compression side at $0.5L_c$ is deformed more flatten than $0.25L_c$ and $0.75L_c$.

Figure 8(e) demonstrates a PPR cylinder form by honeycomb cell with a maximum 6.8 degrees elastic rotation range which is 3.5 times smaller than cylindrical metamaterial with helical cells. Unlike other cylinders, the maximum and minimum diameter strain values at $0.1L_c$ and $0.9L_c$ are both positive, while the positive strain values are larger than the negative strain values for the rest of the measuring points. Furthermore, the magnitude of the minimum diameter strain value at $0.1L_c$ and $0.9L_c$ has an increasing trend until 6.6 degrees, then reduces until structure failure. The maximum positive diameter strain is measured at $0.1L_c$ at 6.8 degrees with a value of 0.04, which is four times larger than cylindrical helical cell metamaterial at the same rotation angle. Furthermore, the maximum magnitude of the negative diameter strain value is -0.01 at $0.4L_c$ at 6.8 degrees, which is 1.7 times larger than

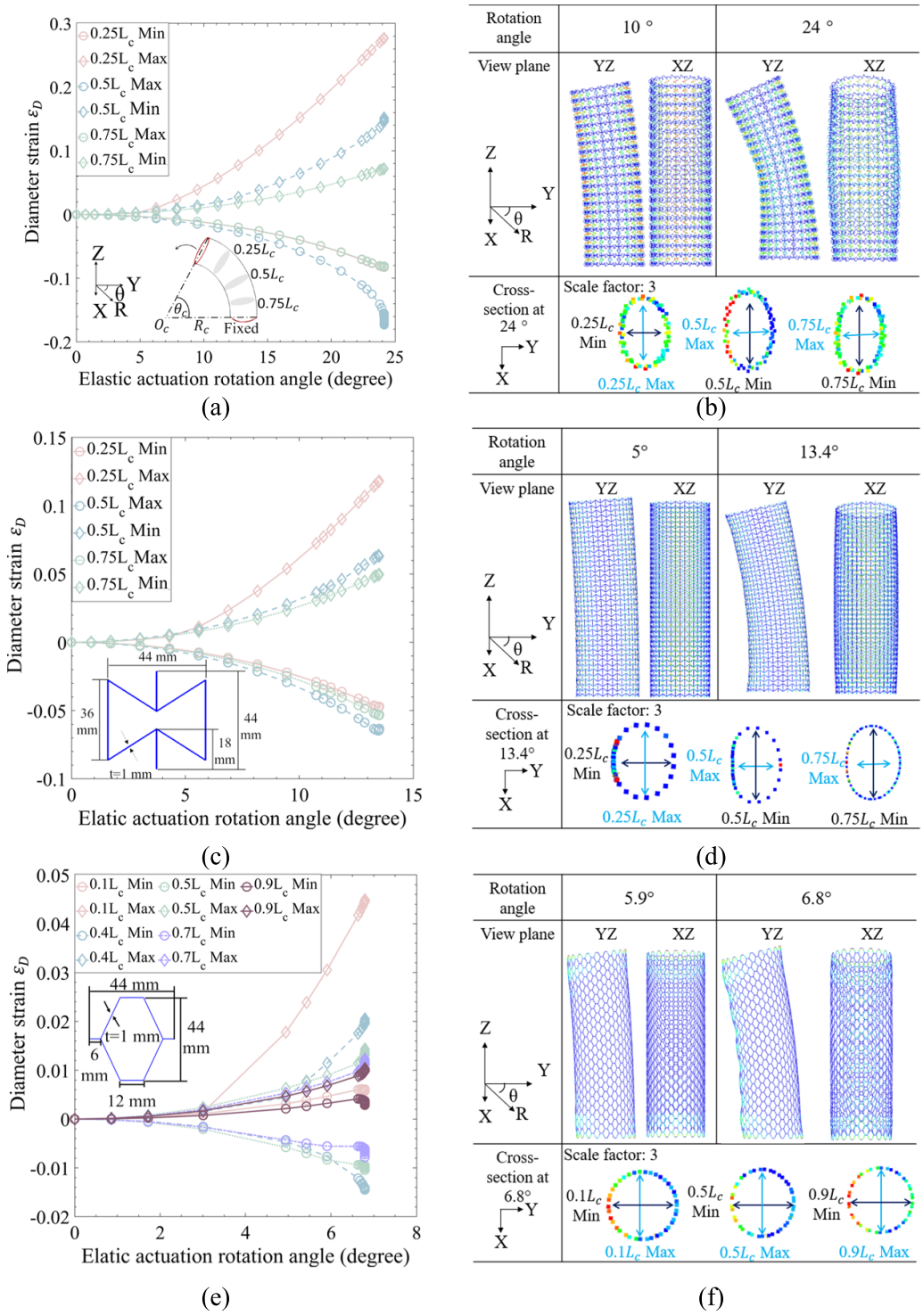

Figure 8. Shape morphing under global bending actuation, (a) diameter strain as a function of elastic actuation rotation angle for zero Poisson's ratio cylindrical helical cell metamaterial, (b) deformation for zero Poisson's ratio cylindrical helical cell metamaterial, (c) diameter strain as a function of elastic actuation rotation angle for negative Poisson's ratio with re-entrant cell, (d) deformation for negative Poisson's ratio cylinder with re-entrent cell, (e) diameter strain as a function of elastic actuation rotation angle for positive Poisson's ratio with honey combe cell, (f) deformation for positive Poisson's ratio cylinder with honeycomb cell.

the maximum negative diameter strain for cylindrical helical cell metamaterial at identical rotation angle.

Figure 8(f) illustrates the deformation for the global bending of the PPR cylinder with honeycomb cell. Local buckling behaviour under bending with significant humps is formed at the top and bottoms in the compression side at a rotation angle 5.9 degrees in *YZ* plane. Moreover, there is no significant diameter change at rotation angle 5.9 in *XZ* plane. In *YZ* plane view at rotation 6.8 degrees, the compression side has corrugation deformation from top to bottom of the cylinder

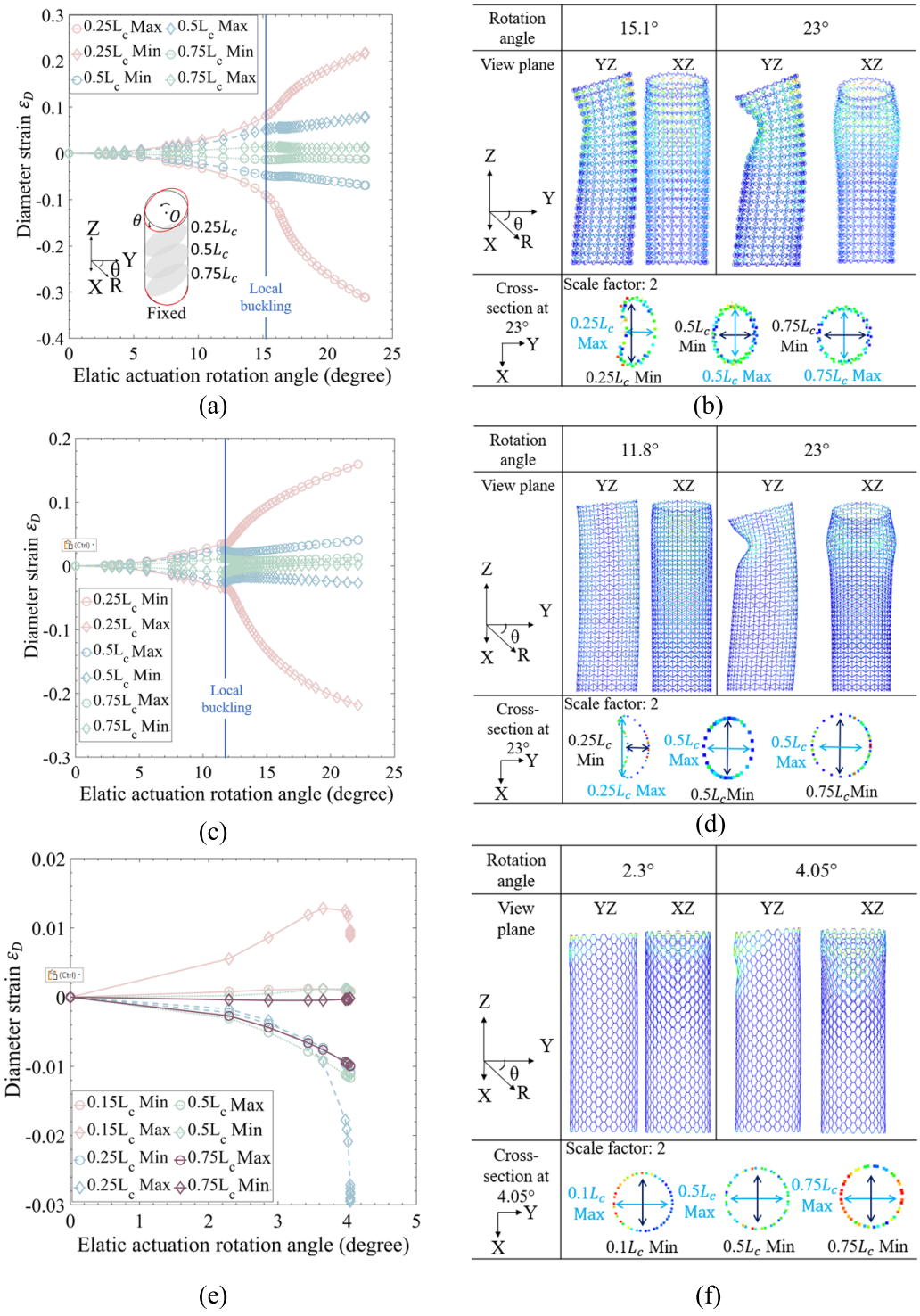

Figure 9. Shape morphing under local bending, (a) diameter strain as a function of elastic actuation rotation angle for zero Poisson's ratio cylindrical helical cell metamaterial, (b) deformation for zero Poisson's ratio cylindrical helical cell metamaterial, (c) diameter strain as a function of elastic actuation rotation angle for negative Poisson's ratio with re-entrant cell, (d) deformation for negative Poisson's ratio cylinder with re-entrant cell, (e) diameter strain as a function of elastic actuation rotation angle for positive Poisson's ratio with honeycomb cell, (f) deformation for positive Poisson's ratio cylinder with honeycomb cell.

and the tension side has small depression trends at top and bottom of the cylinder. The cylinder sides from *XZ* plane view are smoother than in YZ view. Nevertheless, the cross-section shape of the cylinder remains circular at $0.15L_c$ and $0.5L_c$ at rotation angles up to 6.8 degrees. The cross-section shapes with an actuation rotation angle 6.8 degrees at all measuring locations remain circular and exaggerated with scale factor three. Unlike other cylinders, the minimum diameter strains are measured along *Y* axis, while the maximum diameter strains are measured along *X* axis.

8.2. Theta rotation actuation

Figure 9 demonstrates the shape morphing under theta rotation actuation for ZPR, PPR and NPR cylinders. Figure 9(a) presents the boundary condition for theta rotation actuation with a fixed cylinder bottom and applies rotation along X axis at the centre point (O) on the top cylinder. The measuring points for ZPR and NPR cylinders are identical to the global bending actuation case study, however, measuring points located at $0.15L_c$, $0.25L_c$, $0.5L_c$, $0.75L_c$ are considered for PPR cylinder.

Figure 9(a) presents the diameter strain as a function of theta rotation actuation angle with different measuring location for cylindrical helical cell metamaterial with an elastic 23 degrees rotation until large local buckling behaviour. The magnitude of diameter strain at all measuring locations increases with rotation angle increases. Unlike global bending actuation, the maximum magnitude for positive and negative diameter strains is located at $0.25L_c$ with values of 0.21 and -0.31 at rotation angle 23 degrees, respectively. Furthermore, local buckling causes large non-linear increments for diameter strain to start at 15.1 degrees. Figure 9(b) illustrates the deformation for the theta rotation actuation of cylindrical metamaterial with helical cell. A bending behaviour with a reduction of diameter at around $0.25L_c$ is observed at rotation angle 15.1 degrees in YZ plane, while an increasing diameter is observed at the exact location in XZ plane. Finally, from 15.1 to 23 degrees, local buckling with diameters massively decrease at the compression side of $0.25L_c$ and form a depression shape in YZ plane. In XZ plane view, the strain increment can be observed with hump shapes at location $0.25L_c$. The cross-sections for all measuring locations at 23 degrees are presented with scale factor two. It is noticed that the cross-section at $0.25L_c$ deforms into a crescent shape, while maximum and minimum diameter strains are measured along Y and X axis. The cross-section at $0.5L_c$ becomes oval shape and cross-section remains circular at $0.75L_c$, where the minimum and maximum diameter strains are measured along Y and X axis.

Figure 9(c) presents the NPR cylinder under theta rotation actuation with 23 degrees elastic actuation rotation range. The diameter strains increase with rotation angle before 11.8 degrees. After 11.8 degrees, the diameter strains for $0.25L_c$, maximum strain value at $0.5L_c$ and $0.75L_c$ are increasing with rotation angle increases, while the minimum diameter strain at $0.5L_c$ and $0.75L_c$ decreases with diameter decrease. Furthermore, all diameter strain trends from zero to 11.8 degrees show smooth non-linear behaviour, while the trends from 11.8 to 22 degrees have massive non-linear changes due to local buckling. For all measuring points except $0.25L_c$, the positive diameter strain value is greater than the negative strain value. Thus, the maximum positive and negative diameter strain values at 11.8 degrees are 0.04 and -0.03 at $0.25L_c$, where the positive strain value is identical and the negative strain value is 1.7 times smaller than cylindrical helical cell metamaterial. Figure 9(d) illustrates the deformation for the theta rotation actuation of the NPR cylinder formed by re-entrant cells. Bending behaviour with no significant local buckling is observed with a rotation angle 11.8 degrees in YZ and XZ planes. A significant local buckling at compression side $0.25L_c$ in YZ plane can be viewed at 23 degrees. In XZ plane view, the strain increment can be observed with hump shapes at location $0.25L_c$ at actuation 23 degrees. The cross-sections for all measuring locations at 23 degrees are presented with scale factor two. The cross-section at $0.25L_c$ deforms into a crescent shape, while $0.5L_c$ becomes oval shape and cross-section remains circular at $0.75L_c$. Unlike helical cell metamaterial, the maximum and minimum diameter strains locate at $0.25L_c$ measure along X and Y axis. Moreover, the maximum and minimum diameter strains locate at $0.5L_c$ and $0.75L_c$ are measuring along Y and X axis.

Figure 9(e) demonstrates a PPR cylinder with a maximum 4.05 degrees elastic rotation angle which is 5.9 times smaller than cylindrical helical cell metamaterial. The deformation for the PPR cylinder is more complicated than other cylinders. The maximum and minimum diameter strains for $0.15L_c$ and $0.25L_c$ are with positive and negative values, respectively. The maximum diameter strain for diameter strain at $0.5L_c$ and $0.75L_c$ are with positive values, while the minimum diameter strain values are negative. It is noticed that the maximum diameter strain at $0.15L_c$ decreases sharply at a rotation angle 4.0 degrees, and the minimum diameter strain at $0.25L_c$ increase massively at the same rotation angle. The non-linear behaviour for all diameter strains occurs after an actuation angle 2.3 degrees due to the local buckling happens. Furthermore, the maximum and minimum diameter strain values at rotation angle 2.3 degrees are 0.006 and -0.003 at $0.15L_c$ and $0.5L_c$, which is around 4.6 and 2.1 times larger than cylindrical helical cell metamaterial. The maximum and minimum diameter strain values at an elastic rotation angle 4.05 degrees are 0.009 and -0.03 at $0.25L_c$ and $0.5L_c$, which is approximately two and 5.9 times larger than cylindrical helical cell metamaterial. Figure 9(f) illustrates the deformation mechanism for the theta rotation actuation of the PPR cylinder formed by honeycomb cells. Bending behaviour with local deformations observed at 2.3 degrees with a small hump form at the compression side at $0.15L_c$ in YZ plane view, no significant local deformation shows in XZ plane.

Furthermore, the corrugation shape formed from $0.15L_c$ to $0.25L_c$ at compression sides at rotation angle 4.05 degrees, while tinny curvature at the tension side can be seen in YZ plane and no local deformation is observed in XZ plane. The cross-section shape with an actuation rotation angle 4.05 degrees at all measuring locations remains circular and exaggerated with scale factor two. It is noticed that the maximum diameter strains are measured along Y axis and all minimum values are measured along X axis at all measuring locations.

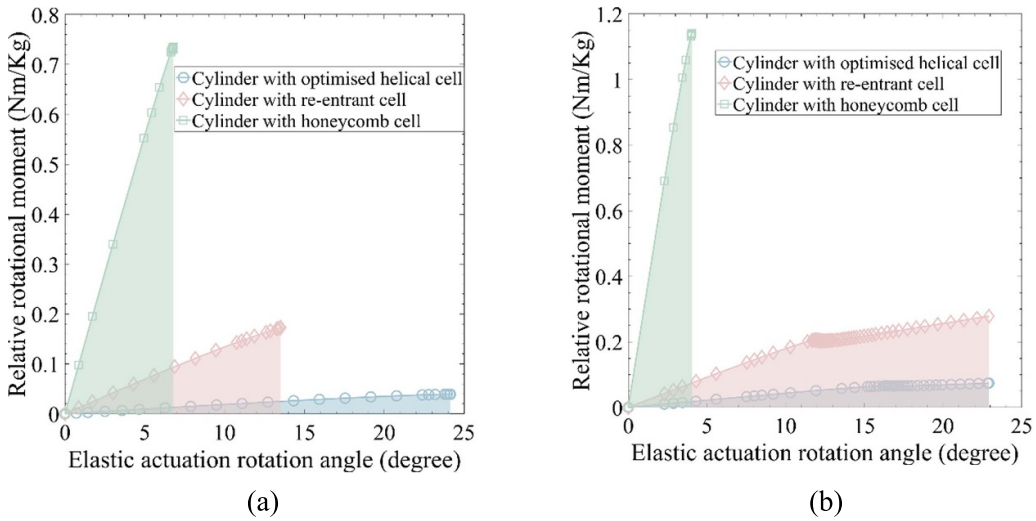

Figure 10. Relative rotational moment as a function of elastic actuates rotation angle for cylindrical helical cell metamaterial, cylinder with re-entrant cell and cylinder with honeycomb cell, (a) under global bending, (b) under local bending.

8.3. Bending actuation energy

Morphing applications require low actuating force to minimise the deformation complexity. Thus, figure 10 demonstrates relative rotation moments as a function of actuation rotation angle investigated and compared between cylindrical optimised spring metamaterial, NPR with re-entrant cylinder and positive Poisson's ratio cylinder with honeycomb cell with two case studies. Furthermore, the relative rotational moment is normalised by the cylinder mass. Moreover, the tinted areas under the curves demonstrated the relative energy required for actuation.

Figure 10(a) presented the relative rotational moment required under global bending actuation, increasing with rotational angle increases. The cylindrical helical cell metamaterial has a maximum actuating relative moment with the value of 0.039 Nm Kg^{-1} at rotation angle 24 degrees which is 18.7 times smaller than cylinder with honeycomb cell at rotation angle 6.8 degrees and 4.4 times less than cylinder with re-entrant cell at rotation angle 13.4 degrees. Moreover, the areas under the curvatures present the cylindrical metamaterial with helical cell requires relative energy 0.52 J Kg^{-1} to the maximum elastic actuation rotation angle, cylinder with re-entrant cell has relative energy 1.23 J Kg^{-1} at a maximum elastic actuation rotation angle 13.4, which is 6.45 times larger than cylindrical metamaterial with helical cell at identical rotation angle. The relative energy for the cylinder with honeycomb at maximum elastic actuation rotation angle 6.8 degrees with value 2.57 J Kg^{-1} is 69.45 times larger than cylindrical metamaterial with helical cell at identical rotation angle.

Similarly, the relative rotation moment in figure 10(b) for all cylinders increases with rotation angle increases under theta rotation actuation. The maximum relative rotational moment for cylindrical helical cell metamaterial is 0.074 Nm Kg^{-1} at 24.05 degrees, which is 3.6 times less than a cylinder with re-entrant cell at a similar rotation angle and 15.4 times smaller than cylinder with honeycomb cell at rotation angle 4.04 degrees. Furthermore, the areas under the curvatures present the cylindrical metamaterial with helical cells requiring relative energy 1.03 J Kg^{-1} to the maximum elastic actuation rotation angle, which is 3.79 smaller than cylinders with re-entrant cell at identical rotation angle. Cylinder with honeycomb cell has relative energy 2.42 J Kg^{-1} at a maximum elastic actuation rotation angle 3.9 degrees, which is 92 times larger than cylindrical metamaterial with helical cell with identical rotation angle.

Considering all mechanical behaviours investigated above, ZPR cylindrical helical cell metamaterial is more suitable for morphing applications, as it has more flexibility and requires less actuating force and energy required. Similar to other shell cylinders [34], ZPR cylindrical helical cell metamaterial, re-entrant cell cylinder, honeycomb cylinder exhibit Brazier effect with ovalised cross-section, however, the ZPR cylindrical helical cell metamaterial has lowest Brazier effect among them. Although the local bending elastic rotation angle assigned to the cylindrical helical cell and cylinder with re-entrant cell are identical, the local buckling behaviour happen at 16.4 and 11.8 degrees for cylindrical helical cell and cylinder with re-entrant cell, respectively. Moreover, cylindrical helical cell metamaterial with maximum stress 3.8 MPa is almost twice smaller as the cylinder with re-entrant cell under local bending 23 degrees rotation angle.

9. Conclusion

In this paper, novel cylindrical metamaterial with helical cell exhibiting ZPR in multiple directions were introduced for the

first time in literature. Fine-fidelity CAD models were created with 'wrap curve' function in CATIA. a Significant number of FEA simulations with fine mesh were performed on high performance computing servers for different tessellation models to investigate the mechanical behaviours of the cylindrical metamaterial. Finite element simulations with beam elements demonstrated the homogenised behaviour and ideal value of Poisson's ratios, torsion and normalised Young's modulus for different tessellation numbers, while FEA models with solid elements demonstrated the reliable deformation mechanism and stress distribution in realistic cases. Buckling and modal behaviour of cylindrical metamaterial with optimised spring element were studied and compared with equivalent shell cylinders, highlighting lower range of eigenvalue than equivalent shell cylinder due to the lower stiffness of cylindrical metamaterial. Different tessellation homogeneity created unique and complicated buckling and vibration mode shapes due to bending and torsion features. The cylindrical models were specifically manufactured using SLS 3D sprinting technology due to the complex curvatures of the model. Tensile experiments were performed to validate Poisson's ratio and deformation mechanism between the experiment and numerical models. The excellent correlation of results demonstrated the reliability of numerical models for future study. Furthermore, the shape morphing analysis with two case studies are investigated and compared with equivalent positive and NPR cylinders. Moreover, the energy required for actuation was also discussed and showed a lower energy requirement than equivalent negative and positive Poisson's ratio cylinders. The results show excellent potential integration of this cylindrical metamaterial due to ZPR in cylindrical systems for further realisation of medical stents, soft robotics and engine inlet lip advances.

Data availability statement

All data that support the findings of this study are included within the article (and any supplementary files).

Appendix A

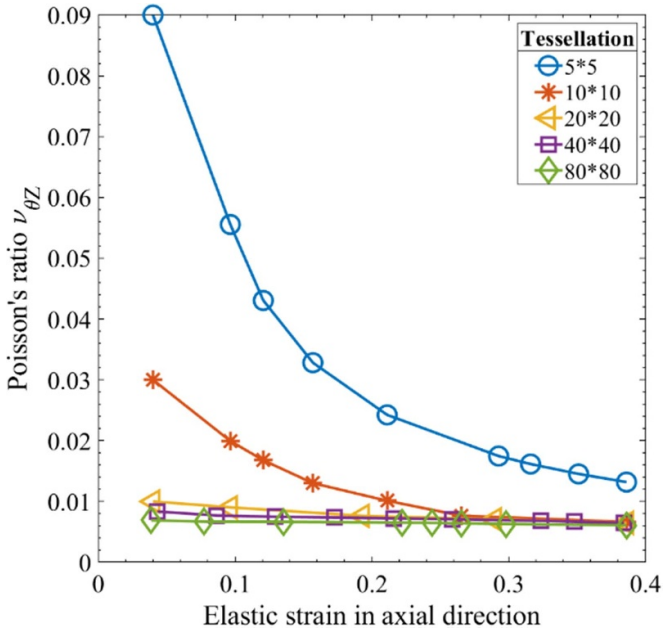

Figure A. Homogenisation of Poisson's ratio $\nu_{\theta Z}$ with different tessellation numbers for cylindrical zero Poisson's ratio helical cell metamaterial.

Appendix B

Buckling Load	Mode shape
91.363N	

Figure B. Buckling load and mode shape for equivalent shell cylinder.

ORCID iD

Qing Qin https://orcid.org/0000-0003-4616-4572

Reference

[1] Bonfanti S, Guerra R, Font-Clos F, Rayneau-Kirkhope D and Zapperi S 2020 Automatic design of mechanical metamaterial actuators *Nat. Commun.* **11** 1–10

[2] Li J E and Wang B L 2020 Effect of negative Poisson's ratio on the fracture mechanics parameters due to mechanical and thermal loads *Int. J. Eng. Sci.* **150** 1–11

[3] Mohsenizadeh S, Alipour R, Shokri Rad M, Farokhi Nejad A and Ahmad Z 2015 Crashworthiness assessment of auxetic foam-filled tube under quasi-static axial loading *Mater. Des.* **88** 258–68

[4] Xu T and Li G 2011 A shape memory polymer based syntactic foam with negative Poisson's ratio *Mater. Sci. Eng.* A **528** 6804–11

[5] Neville R M, Monti A, Hazra K, Scarpa F, Remillat C and Farrow I R 2014 Transverse stiffness and strength of Kirigami zero-ν PEEK honeycombs *Compos. Struct.* **114** 30–40

[6] Olympio K R and Gandhi F 2010 Zero Poisson's ratio cellular honeycombs for flex skins undergoing one -dimensional morphing *J. Intell. Mater. Syst. Struct.* **21** 1737–53

[7] Gaal V, Rodrigues V, Dantas S O, Galvão D S and Fonseca A F 2020 New zero Poisson's ratio structures *Phys. Status Solid* **14** 4–7

[8] Soman P, Fozdar D Y, Lee J W, Phadke A, Varghese S and Chen S 2012 A three-dimensional polymer scaffolding material exhibiting a zero Poisson's ratio *Soft Matter* **8** 4946–51

[9] Yang H and Ma L 2018 Multi-stable mechanical metamaterials with shape-reconfiguration and zero Poisson's ratio *Mater. Des.* **152** 181–90

[10] Gong X, Huang J, Scarpa F, Liu Y and Leng J 2015 Zero Poisson's ratio cellular structure for two -dimensional morphing applications *Compos. Struct.* **134** 384–92

[11] Naghavi Zadeh M, Dayyani I and Yasaee M 2020 Fish cells, a new zero Poisson's ratio metamaterial—part I: design and experiment *J. Intell. Mater. Syst. Struct.* **31** 1617–37

[12] Jha A and Dayyani I 2021 Shape optimisation and buckling analysis of large strain zero Poisson's ratio fish-cells metamaterial for morphing structures *Compos. Struct.* **268** 113995

[13] Miller T F, Gandhi F S and Rufino R J 2014 Morphing hull concept for underwater vehicles *Ocean Eng.* **92** 92–102
[14] Haga Y, Muyari Y, Goto S, Matsunaga T and Esashi M 2011 Development of minimally invasive medical tools using laser processing on cylindrical substrates *Electr. Eng. Japan* **176** 65–74
[15] Bhullar S K, Lekesiz H, Karaca A A, Cho Y, Willerth S M and Jun M B G 2022 Characterizing the mechanical performance of a bare-metal stent with an auxetic cell geometry *Appl. Sci.* **12** 910
[16] McKenna C G and Vaughan T J 2021 A finite element investigation on design parameters of bare and polymer-covered self-expanding wire braided stents *J. Mech. Behav. Biomed. Mater.* **115** 104305
[17] Liu J and Zhang Y 2018 Soft network materials with isotropic negative Poisson's ratios over large strains *Soft Matter* **14** 693–703
[18] Wei K, Peng Y, Qu Z, Zhou H, Pei Y and Fang D 2018 Lightweight composite lattice cylindrical shells with novel character of tailorable thermal expansion *Int. J. Mech. Sci.* **137** 77–85
[19] Wei K, Xu W, Ling B, Yang X and Fang D 2021 Multi-functional cylindrical metastructures to simultaneously program both thermal expansion and Poisson's ratio *Extrem. Mech. Lett.* **43** 101177
[20] Wei K, Yang Q, Ling B, Qu Z, Pei Y and Fang D 2018 Design and analysis of lattice cylindrical shells with tailorable axial and radial thermal expansion *Extrem. Mech. Lett.* **20** 51–58
[21] Ling B, Wei K, Qu Z and Fang D 2021 Design and analysis for large magnitudes of programmable Poisson's ratio in a series of lightweight cylindrical metastructures *Int. J. Mech. Sci.* **195** 106220
[22] Gao Q, wang Y, Ma Z-D and Zhong H 2018 Analyses on mechanical properties of the cylindrical double-V micro-structure *SAE Technical Paper* vol 1 pp 1–6
[23] Lorato A, Innocenti P, Scarpa F, Alderson A, Alderson K L, Zied K M, Ravirala N, Miller W, Smith C W and Evans K E 2010 The transverse elastic properties of chiral honeycombs *Compos. Sci. Technol.* **70** 1057–63
[24] Frenzel T, Kadic M and Wegener M 2017 Supplementary materials for three-dimensional mechanical metamaterials with a twist *Science* **358** 1027–32
[25] Ma C, Lei H, Hua J, Bai Y, Liang J and Fang D 2018 Experimental and simulation investigation of the reversible bi-directional twisting response of tetra-chiral cylindrical shells *Compos. Struct.* **203** 142–52
[26] Qin Q, Dayyani I and Webb P 2022 Structural Mechanics of cylindrical fish-cell zero Poisson's ratio metamaterials *Compos. Struct.* **289** 115455
[27] Liu K *et al* 2020 4D printed zero Poisson's ratio metamaterial with switching function of mechanical and vibration isolation performance *Mater. Des.* **196** 109153
[28] Landers M, Hall L, Auman L and Vaughn M 2003 Deflectable nose and canard controls for a fin-stabilized projectile at supersonic and hypersonic speeds *21st AIAA Appl. Aerodyn. Conf.* (American Institute of Aeronautics and Astronautics) (https://doi.org/10.2514/6.2003-3805)
[29] Chen P C, Sulaeman E, Liu D and Auman L 2003 Body-flexure control with smart actuation for hypervelocity missiles *44th AIAA/ASME/ASCE/AHS/ASC Structures, Structural Dynamics and Materials Conf.* (American Institute of Aeronautics and Astronautics) pp 1–11
[30] Chapkin W A, Walgren P, Frank G J, Seifert D R, Ward Rashidi M R, Hartl D J and Baur J W 2020 Bending mechanics of cylindrical skins for morphing aerospace applications *Mater. Des.* **186** 108316
[31] Chapkin W A, Walgren P, Frank G J, Seifert D R, Hartl D J and Baur J W 2020 Design and optimization of high-strain, cylindrical composite skins for morphing fuselages *Mater. Des.* **187** 108395
[32] Cimolai G, Dayyani I and Qin Q 2022 Multi-objective shape optimization of large strain 3D helical structures for mechanical metamaterials *Mater. Des.* **215** 110444
[33] Qin Q and Dayyani I 2023 Large strain zero Poisson's ratio spring cell metamaterial with critical defect analysis and variable stiffness distributions *Compos. Struct.* **318** 117102
[34] Tatting B F, Gürdal Z and Vasiliev V V 1997 The Brazier effect for finite length composite cylinders under bending *Int. J. Solids Struct.* **34** 1419–40

2023-09-22

Cylindrical helical cell metamaterial with þÿ l a r g e s t r a i n z e r o P o i s s o n s r a shape morphing analysis

Qin, Qing

IOP Publishing

þÿ Q i n Q , D a y y a n i I . (2 0 2 3) C y l i n d r i c a l h e l i c a l c e l l m e t a m a t e r i a l w i t h l a r g e ratio for shape morphing analysis. Smart Materials and Structures, Volume 32, Issue 10, October 2023, Article number 105039

https://doi.org/10.1088/1361-665X/acf96c